

Interconnected Phosphorus and Nitrogen Codoped Porous Exfoliated Carbon Nanosheets for High-Rate Supercapacitors

Jutao Jin,[†] Xiaochang Qiao,[†] Feng Zhou,[‡] Zhong-Shuai Wu,[‡] Lifeng Cui,^{*,†} and Hongbo Fan^{*,†}

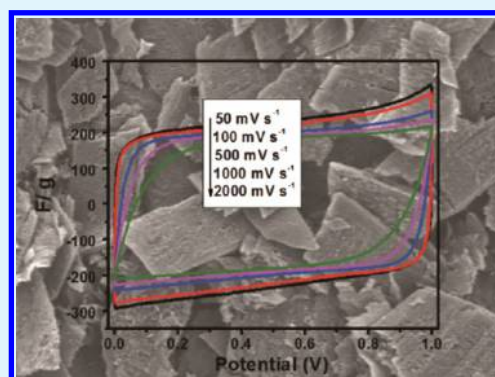
[†]School of Environment and Architecture, Dongguan University of Technology, Daxue Road No. 1, Songshan Lake High-Tech Development, Dongguan 523808, P. R. China

[‡]Dalian National Laboratory for Clean Energy, Dalian Institute of Chemical Physics, Chinese Academy of Sciences, 457 Zhongshan Road, Dalian 116023, P. R. China

S Supporting Information

ABSTRACT: Carbon-based supercapacitors have high power density and long cycle life; however, they are known to suffer from problems related to low energy density and high inner resistance. Here, we report a novel hierarchically porous functional carbon that is made up of interconnected exfoliated carbon nanosheets with thickness of a few nanometers. Notably, these porous carbon nanosheets are doped with abundant nitrogen (N) dopants in the basal plane and phosphorus (P) functional groups at the edge of the graphene lattice. The specific surface chemistry and pore structure of the synthesized sample, combined with its large specific surface area, make it a high-performance active material for supercapacitor electrode. The obtained supercapacitor made with the optimized sample showed a high specific capacitance (265 F g^{-1} at 0.5 A g^{-1}) as well as long-term stability (94% capacitance retention after 5000 cycles). Particularly, the enhanced electrochemical characteristics were maintained even at high electrode mass loading (time constant (τ_0) is 1.10 s for an electrode mass loading of 12.38 mg cm^{-2} compared to 1.61 s for a mass loading of 4.17 mg cm^{-2} for commercial activated carbon), which is important for a high packing factor of the capacitor.

KEYWORDS: phosphorus and nitrogen codoped, exfoliated carbon nanosheets, high rate, supercapacitor, cycle stability



1. INTRODUCTION

Carbon-based supercapacitors, ideal energy-storage devices for fast storage and release of energy, have attracted great attentions for energy management in the future electricity-powered world.¹ Although these energy-storage devices are featured with characteristics of high power density and long cycle life, their widespread applications are still limited by their low energy-storage density and high series resistance. One of the main challenges in the development of supercapacitors is to optimize the energy density without deteriorating their high power capability, as these two parameters determine the ultimate performance of the supercapacitor. The development of high-performance electrode-active materials is a key factor to ensure both high energy and power densities.^{2–10}

In a supercapacitor, energy is stored at the electrode–electrolyte interface through the adsorption of ions from solution at charged porous electrodes.¹¹ Its capacitance performance strongly depends on the accessible surface area and the wetting behavior of the electrode surface with the electrolyte. Meanwhile, its power property is intimately related to the internal resistance from ion transportation and electron conductivity. Thus, the specific surface area and pore structures of the porosity structure^{6,10–16} and the nature of the resulting carbon materials, including their purification, graphitization degree, concentration of dopants, and their doping structure in

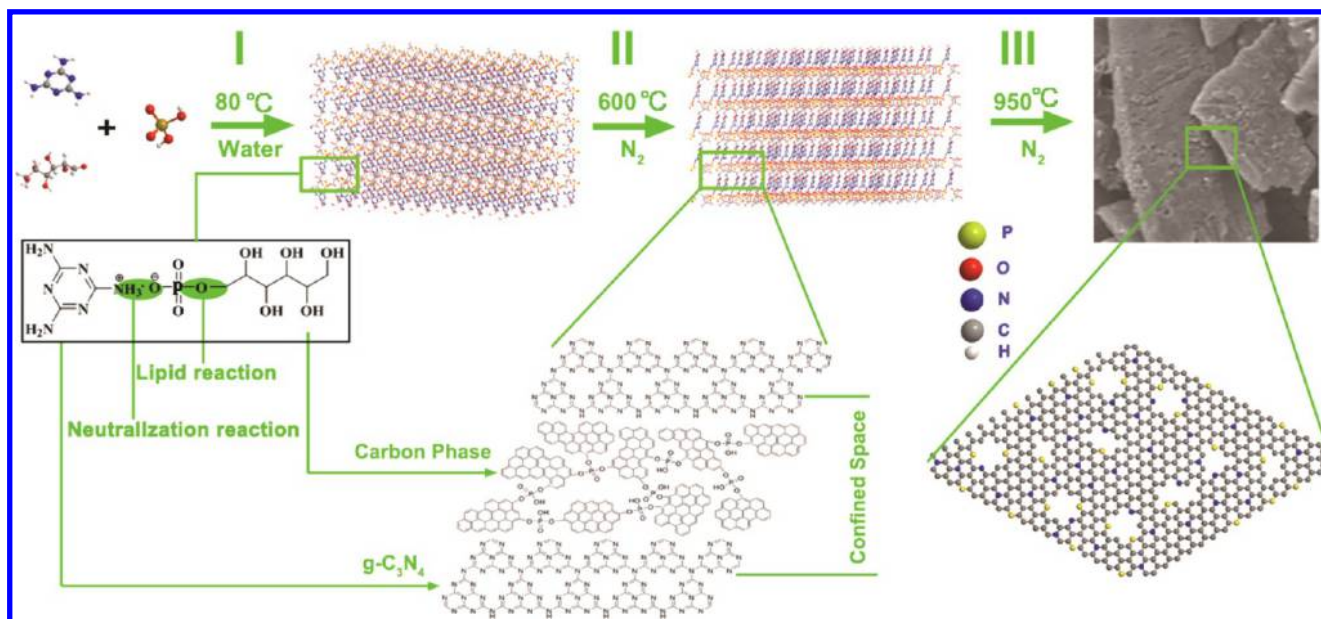
the carbon lattice, are the main concerns for the development of high-performance electrode-active materials.^{5,7,19–26} Traditional porous activated carbons (ACs), with a high specific surface area of up to $3000 \text{ m}^2 \text{ g}^{-1}$, has gravimetric capacitances of only about 200 and 100 F g^{-1} in aqueous and organic electrolytes, respectively, because of the difficulty faced by the electrolyte ions to efficiently access the micropore surfaces.^{27,28} Furthermore, the high internal resistance induced by their poor electronic conductivity and long ion-transport pathway severely affects the rate performances and power density of the assembled capacitors. Recently, hierarchical porous carbon materials constructed with novel carbon nanomaterials, including graphene and carbon nanotubes, have been strongly recommended for the fabrication of advanced supercapacitors.^{2,12,13,15–18,29–37} Furthermore, doping and/or surface functionalization can further boost their intrinsic performances by affording pseudocapacitance or improving their wetting property with electrolyte.^{3,22,25,38}

Lately, we present a novel P/N-codoped hierarchical porous carbon constructed with crumple-thin carbon layers, which are doped with abundant nitrogen dopants in the basal plane and

Received: January 13, 2017

Accepted: May 3, 2017

Published: May 3, 2017

Scheme 1. Schematic Illustration of the Synthesis Procedure for PN-ECB^a

^a(I) Synthesis of MPG precursor in water solution. (II) Formation of sandwiched carbon and carbon nitride layer composite at moderate temperature (600 °C). (III) Formation of PN-ECB at high temperature (above 700 °C).

phosphorus functional groups at the edges of graphene lattice.³⁹ These thin graphite layers are regularly aligned and interlocked together to form open porous structures between these interconnected neighboring interlayer spaces. The unique structure of the sample satisfies the critical requirements for an ideal supercapacitor electrode. The large specific surface area and the open porous framework formed by the well-defined neighboring interlayer space of porous thin graphite walls as well as high concentrations of dopants in the carbon lattice not only provides a large electrode–electrolyte interface for electrochemical reaction but also reduces the diffusive resistance by affording short pathways for ion transport. The obtained supercapacitor made with the optimized sample showed a high specific capacitance (265 F g⁻¹ at 0.5 A g⁻¹) and long-term stability (94% capacitance retention after 5000 cycles). Particularly, the enhanced electrochemical characteristics were maintained even at high electrode mass loading, which is important for a high packing factor of the capacitor.

The synthesis process of exfoliated carbon nanosheets (ECBs) is illustrated in Scheme 1, which includes the fabrication of organic–inorganic precursor melamine/pyrophosphate-glucose ester (MPG) and its subsequent carbonization at high temperature under N₂ atmosphere (see Experimental Section for details of the synthesis). First, phosphoric acid reacts with melamine and glucose through neutralization and lipid reaction in water solution, respectively, to form a white organic–inorganic crystal. The basic unit of these organic–inorganic crystals is a melamine–phosphoric acid–glucose segment. Here, phosphoric acid functioned as a binder to assemble melamine and glucose at molecular scale through ionic bond and P–O–C ester bond, respectively. This is a key for the subsequent carbonization process, as it can facilitate the formation of a uniform template–carbon precursor interface. Second, the resulted sample is annealed at a moderate temperature (600 °C) for 2 h. At this stage, MPG is subjected to a phase-separation process: the melamine part is polymerized to a two-dimensional carbon nitride polymer,

whereas the glucose part is carbonized on these carbon nitride layers to form a sandwiched structure with alternative carbon and carbon nitride layers. The acidic group plays an important role in the carbonization of glucose and the formation of a uniform interface between the carbon and carbon nitride phases at this stage. First, it functions as an acid catalyst to promote glucose-bond cleavage and cyclization of polyaromatic fragments and bridges these fragments to form a carbonaceous layer. Second, the acidic groups can reduce the carbonaceous–carbon nitride interface energy through the electrostatic interaction between the acidic and ammonia groups. Finally, further increasing the annealing temperature up to 700 °C, the g-C₃N₄ phase is pyrolyzed and pore-rich ECBs are formed. The carbon nitride phase and acid groups serve as a two-dimensional template and molecular template to direct the growth of two-dimensional carbon layers and create in-plane pores in the carbon layers, respectively. The pyrolyzed products of these templates afford abundant heteroatom sources for the homogeneous doping during the high-temperature annealing process. In contrast with the current soft-template and hard-template methods, our method combines pore creation and heteroatom doping in a single step, without any post-treatment procedures.

2. EXPERIMENTAL SECTION

2.1. Chemicals. Melamine (99%), phosphoric acid (H₃PO₄) (>85%), glucose (>99%), and potassium hydroxide (KOH) (>85%) were purchased from Sigma-Aldrich. All chemicals were used as received, without any further purification.

2.2. Synthesis of P/N-Codoped Porous ECBs. Melamine (5.3 g) and glucose (0.25 g) were dissolved in deionized water (200 mL) at 80 °C, and the solution was stirred for 1 h. Then, phosphoric acid (1.43 mL) was added to the above solution dropwise. A white solid precipitated quickly from the transparent solution to form a sticky mixture. The mixture was vacuum-dried using a rotary evaporator to get white solid powder. The dried samples were carbonized at various temperatures of 750, 850, and 950 °C for 2 h under N₂ atmosphere at a heating rate of 5 °C min⁻¹. After cooling to room temperature, the

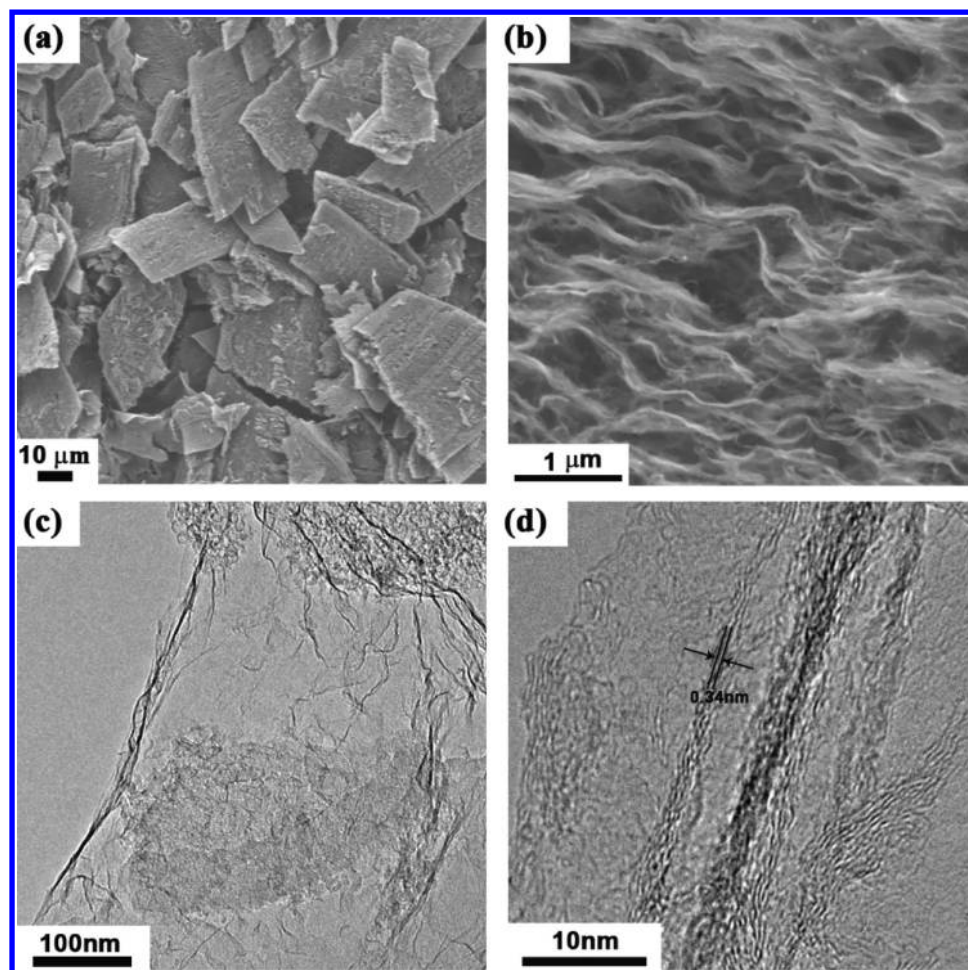


Figure 1. Structural and compositional analysis of as-prepared ECB samples. (a) Low-resolution SEM image and (b) high-resolution SEM image of PN-ECB-950; (c) low-resolution TEM and (d) HRTEM image of PN-ECB-950.

synthesized samples were collected for further characterization. For comparison, N-doped carbon sheets were prepared with the same procedure, without adding H_3PO_4 to the carbon precursors. For simplicity, samples synthesized at various temperatures were labeled as PN-ECB-T, where “T” refers to the applied annealing temperature, whereas the N-doped carbon sheet was labeled as N-ECB-T.

2.3. Sample Characterizations. Scanning electron microscopy (SEM) images were recorded on a JSM-7800F scanning electron microscope; transmission electron microscopy (TEM) and high-resolution transmission electron microscopy (HRTEM) images were collected on a JEM-2100 transmission electron microscope; and nitrogen sorption isotherms were measured at 77 K using a NOVA2000e analyzer. X-ray photoelectron spectroscopy (XPS) image of the catalysts was acquired on an ESCALAB-250Xi XPS instrument using an Al $K\alpha$ X-ray source.

2.4. Electrochemical Measurements. The electrochemical performances of the carbons were measured in a symmetrical two-electrode cell. The electrodes were prepared by pressing a mixture of 85 wt % of the sample, 10 wt % of acetylene black, and 5 wt % of PTFE binder into pellets (9 mm in diameter) and then pressing the pellets on the current collector nickel foam, followed by vacuum drying at 120 °C for 6 h. Electrodes with mass loading varying from 1 to 13 mg cm^{-2} were prepared. The capacitor was assembled into a two-electrode system, in which the two electrodes have the same composition and mass, separated by a polypropylene membrane using 6 mol L^{-1} KOH aqueous solution as an electrolyte. The cyclic voltammetry (CV) and galvanostatic charge–discharge tests were conducted on CHI 760E workstation. The specific capacitance (C_{two}) in a two-electrode cell was obtained as

$$C_{\text{two}} = 4I\Delta t/m_s\Delta V \quad (1)$$

where I is the constant current, Δt is the discharge time, ΔV is the voltage change during the discharge process, and m_s is the total mass of the active material in both electrodes. The direct-current equivalent internal resistance (R_{in}) of the cell can be obtained in continuous charging/discharging by

$$R_{\text{in}} = V_{\text{drop}}/2I \quad (2)$$

This is further used for the calculation of discharge energy densities of the capacitor (E_{average}) and average power densities of the capacitor (P_{average}) as follows

$$E_{\text{average}} = 1/8 C_{\text{two}}(V_{\text{max}} - IR_{\text{in}})^2 \quad (3)$$

$$P_{\text{average}} = I(V - IR_{\text{in}})/2m \quad (4)$$

3. RESULTS AND DISCUSSION

The microstructure and morphology of the synthesized carbon samples were characterized by electron microscopy. Figure 1a presents the low-resolution SEM image of the typical sample, PN-ECB-950, showing block-shape morphology with size of several hundreds of micrometers. Raman and XRD spectroscopy results indicate the presence of pure-carbon phase without other impurities. The broadening of (002) XRD peak and the large I_D/I_G (1.1) value in Raman spectra suggest more defects in the carbon lattice (Figures S1 and S2). The high-resolution SEM image indicates that these carbon particles are composed

of exfoliated carbon layers, which in turn are interconnected together to form an intertwined scaffold (Figure 1b). TEM further reveals the structure of these ECBs. As shown in the TEM image (Figure 1c), the structural units of these carbon samples are wrinkle-rich thin graphite layers. The HRTEM image (Figure 1d) indicates that these entangled thin carbon layers are about 1.5–3.5 nm in thickness, corresponding to 4–10 layers of graphene sheets. The distance between layers of these entangled wrinkles is about 0.34 nm, consistent with the XRD results (Figure S1). For comparison, sample N-ECB-950, which is synthesized without adding phosphoric acid in the precursor, is also exfoliated, but shows an irregular morphology (Figure S3). In contrast, sample PC-950 synthesized without adding melamine in the precursor is not exfoliated and shows bulk morphology (Figure S4). These results confirm the unique role of phosphoric acid as a cross-linker and its effect in retaining the structural integrity during the carbonization process.

The textural properties of these PN-ECB samples were assessed on the basis of nitrogen adsorption/desorption analysis, and the results are summarized in Table 1. Sample

Table 1. Texture Properties of As-Prepared ECB Samples

samples	S_{BET} ($\text{m}^2 \text{g}^{-1}$)	S_{meso} ($\text{m}^2 \text{g}^{-1}$)	V_{total} ($\text{cm}^3 \text{g}^{-1}$)	V_{micro} ($\text{cm}^3 \text{g}^{-1}$)	V_{meso} ($\text{cm}^3 \text{g}^{-1}$)
PN-ECB-750	39	29	0.05	0.02	0.03
PN-ECB-850	561	247	0.95	0.23	0.72
PN-ECB-950	1440	677	1.62	0.67	0.95
N-ECB-950	497	312	1.27	0.20	1.07

PN-ECB-950 shows type-IV adsorption curves (Figure 2a), indicating the presence of micropores and mesopores. The sample exhibits a specific surface area of $1440 \text{ m}^2 \text{g}^{-1}$ and a total pore volume of $1.62 \text{ cm}^3 \text{g}^{-1}$ (Figure 2b), much larger than those of the hard-template-synthesized porous carbons. The pore-size distribution calculated using the nonlocalized density functional theory method shows an average pore size of 4.5 nm (Figure 2c). For comparison, N-ECB-950 shows a Brunauer–Emmett–Teller surface area of $550 \text{ m}^2 \text{g}^{-1}$ and a widely distributed pore structure from 5 to 25 nm. PN-ECB samples synthesized at relative low temperatures were also analyzed, and the results are shown in Figure S4 and Table 1. Sample PN-ECB-750 synthesized at low temperature shows very low specific surface area ($39 \text{ m}^2 \text{g}^{-1}$) and pore volume ($0.05 \text{ cm}^3 \text{g}^{-1}$). With the increase of temperature to $850 \text{ }^\circ\text{C}$, the specific surface area and total pore volume gradually increased to $561 \text{ m}^2 \text{g}^{-1}$ and $0.92 \text{ cm}^3 \text{g}^{-1}$, respectively. Notably, at this

temperature range, the effect of “micropores” on the specific surface area and specific pore volume of PN-ECB is minor and slowly increases with annealing temperature. We propose that the intercalated $\text{g-C}_3\text{N}_4$ layers are the main “pore-formers” at this temperature range, whose pyrolyzation can create interlayer meso/macropores between the leaving carbon layers. Interestingly, a sharp increase in specific surface area was observed for sample PN-ECB-950, which is mainly due to micropores, as confirmed by their much higher gas uptake value at low relative pressure area ($P/P_0 < 0.1$). At this stage, the acidic groups or their evolved components in the carbon lattice serve as secondary molecular pore-formers, and their decomposition can create rich micropores in the in-plane carbon layers. The following composition analysis also shows a sharp P element drop when annealing temperature increased up to $950 \text{ }^\circ\text{C}$.

The surface chemical composition and the binding state of the samples synthesized at various temperatures were investigated by XPS (Figure 3), and the results are summarized in Table S1. Figure 3a shows the XPS survey of PN-ECB-950 and the presence of peaks centered at 132.3, 284.9, 399.2, and 532.2 eV, corresponding to $\text{P}_{2\text{p}}$, $\text{C}_{1\text{s}}$, $\text{N}_{1\text{s}}$, and $\text{O}_{1\text{s}}$, respectively.^{22,38} The compositions of all PN-ECB samples were found to strongly depend on the carbonization temperature, with a high synthesis temperature showing a low heteroatom doping level. PN-ECB samples synthesized at low temperature ($<900 \text{ }^\circ\text{C}$) show a very high heteroatom doping level, and a sharp drop in doping concentration is observed as the annealing temperature increased up to $950 \text{ }^\circ\text{C}$. The bonding configurations of heteroatoms in ECBs were further studied on the basis of high-resolution XPS spectra. For nitrogen, four types of N, including pyridinic-N (398.3 eV), pyrrolic-N (399.5 eV), quaternary-N (400.3 eV), and oxidic-N (402.3 eV),^{40,41} are formed during the annealing process (Figure 3b). Pyridinic-N is the main type of nitrogen for samples synthesized at low temperature, whereas quaternary-N is dominant for samples synthesized at high temperature. The fact that the quaternary-N, referring to nitrogen bonds to three carbon atoms, is more stable than pyridinic N–C that bonds to two carbon atoms at edge may be the main reason for this phenomenon.⁴² For phosphorus, its $\text{P}_{2\text{p}}$ can be deconvoluted into two components, centered at 132.3 and 134.2 eV, respectively (Figure 3c).^{41–44} The component with a band centered at 132.3 eV is attributed to pentavalent tetra-coordinated phosphate (PO_4), whereas the main band centered at 134.2 eV is attributed to P in a higher oxidation state, referring to pyrophosphate groups (PO_3).^{3,41,45} Notably, no C–P bonding signal (centered at 130 eV) appears even for sample PN-ECB-950 synthesized at the highest temper-

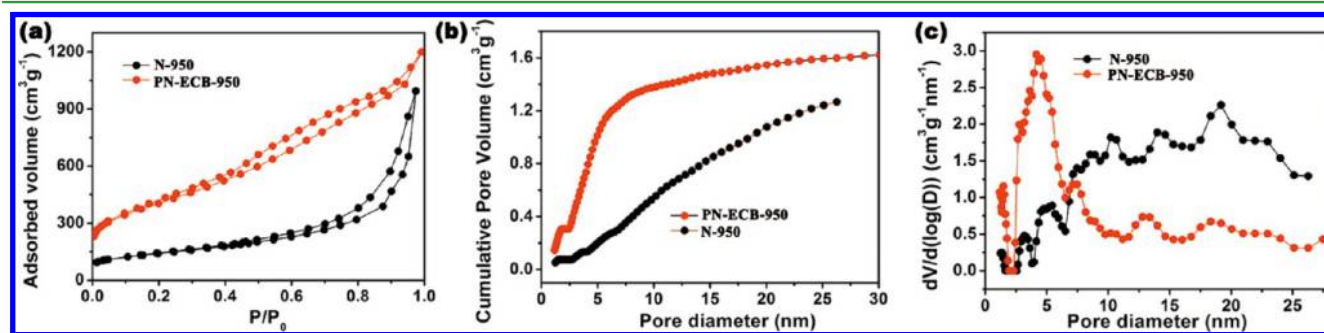


Figure 2. Porosity and composition of PN-ECB-950 and N-950. (a) N_2 adsorption/desorption isotherm of PN-ECB-950 and N-950; (b) cumulative pore volume; and (c) pore-size distribution calculated from N_2 adsorption.

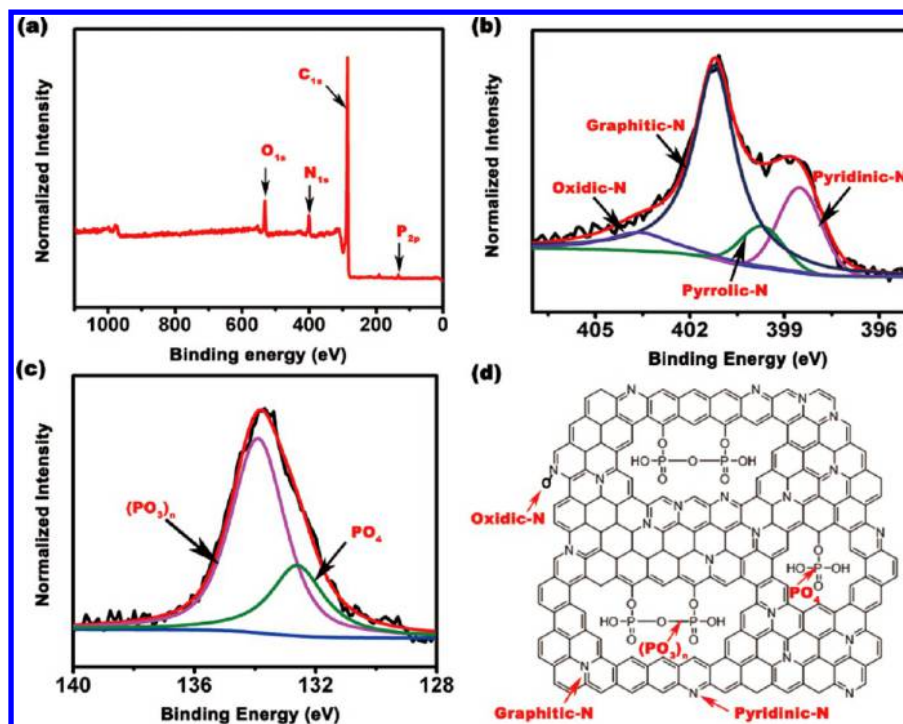


Figure 3. (a) XPS survey spectra of sample PN-ECB-950 and (b, c) high-resolution N_{1s} and P_{2p} of sample PN-ECB-950. (d) Schematic of heterocyclic N and P structures in carbon lattice.

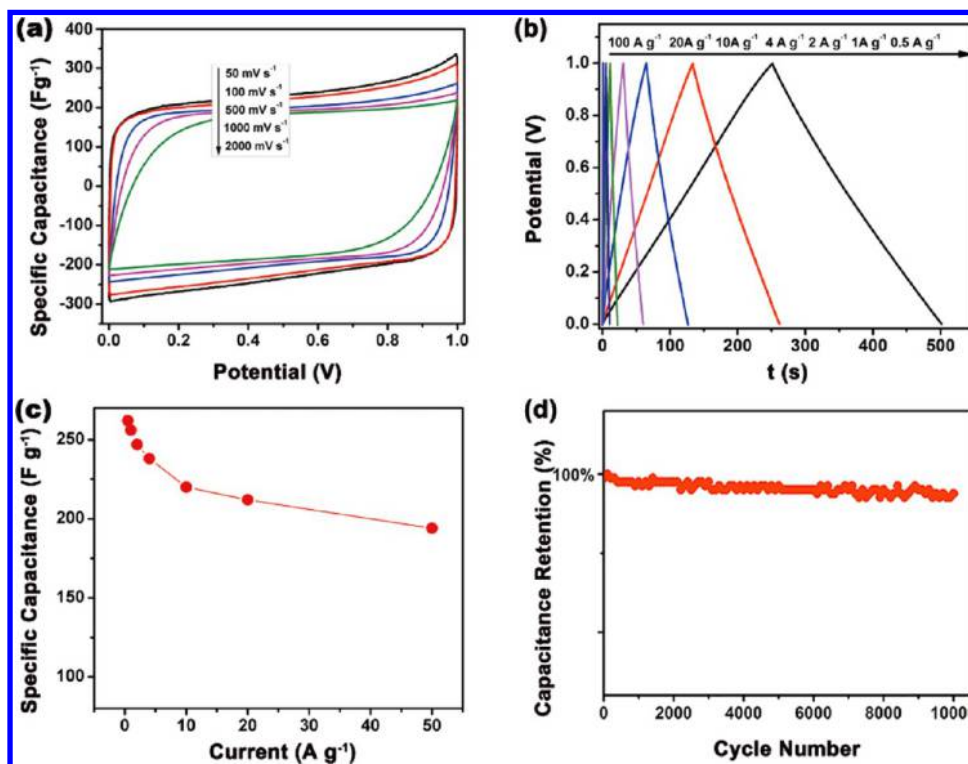


Figure 4. Supercapacitor performances of PN-ECB sample. (a) CV curves of PN-ECB-950 at scan rates from 50 to 2000 mV s^{-1} in a two-electrode cell (electrode mass loading: 1.57 mg cm^{-2}). (b) Galvanostatic charge/discharge curves of PN-ECB-950 at various current densities from 0.5 to 100 A g^{-1} (electrode mass loading: 1.57 mg cm^{-2}). (c) Dependence of specific capacitance of PN-ECB-950 on current density. (d) Long-term stability of PN-ECB-950 after 5000 charge/discharge cycles, at a current density of 5 A g^{-1} . Experiments were conducted in 6 M NaOH solution at 25 $^{\circ}\text{C}$.

ature,^{46,47} suggesting that P atoms are not doped into the graphite lattice but in the form of functional phosphorus groups at the edge site. The detailed structures of P and N are shown in Figure 3d.

3.1. Investigation of ECBs as Electrode Materials for Supercapacitor. The potential applications of the synthesized materials as supercapacitor materials were investigated. Figure 4a shows the CV curves of the PN-ECB-950 electrode in 6.0 M

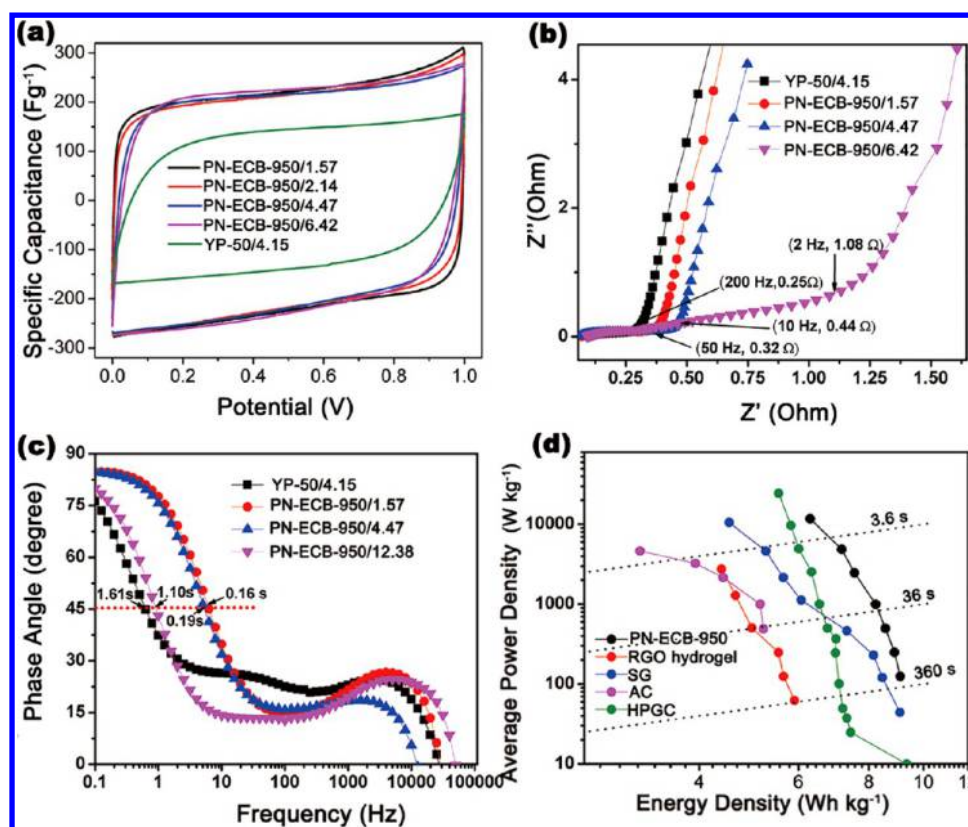


Figure 5. (a) CV curves of commercial AC and PN-ECB-950 with various mass loading at scan rates of 100 mV s^{-1} . (b) Nyquist plot of symmetric supercapacitor based on AC and PN-ECB-950 with different mass loading. (c) Impedance phase angle vs frequency for commercial AC-based supercapacitor and PN-ECB-950-based supercapacitor with low mass loading (1.57 and 2.14 mg cm^{-2} , respectively) and ultrahigh mass loading (12.38 mg cm^{-2}). (d) Comparison of supercapacitor performances based on PN-ECB-950 and other reported high-quality carbon materials for supercapacitor in Ragone plots. Experiments were conducted in 6 M NaOH solution at $25 \text{ }^\circ\text{C}$.

KOH solution with a two-electrode system at scan rates from 50 mV s^{-1} to 2 V s^{-1} . The CV curves maintain almost a rectangular-like shape at scan rate up to 1 V s^{-1} , indicating its good supercapacitor properties and rapid charging/discharging nature. The electrochemical performances of the sample were further studied by galvanostatic charge/discharge measurements in a 6 M KOH aqueous electrolyte. As shown in Figure 4b, sample PN-ECB-950 exhibits nearly triangular-shaped charge/discharge curves, without obvious IR drop at various current densities from 0.5 to 50.0 A g^{-1} , further demonstrating its excellent capacitive behavior and high rate capability. Notably, the charge/discharge curves slightly deviate from the traditional linear sloping potential profiles, suggesting the occurrence of Faradaic process on the surface of PN-ECB-950.⁷ The specific capacitance of PN-ECB-950 at various scan rates was calculated and is shown in Figure 4c. The specific capacitance of our material reached almost 265 F g^{-1} at a charge rate of 0.5 A g^{-1} and maintained a capacitance of above 189 F g^{-1} at a charge rate of 50 A g^{-1} . For comparison, the N-ECB-950 sample shows a relatively lower specific capacitance. We propose that this disparity is mainly due to differences in their wetting properties. The acidic functional groups at the carbon edge of sample PN-ECB-950 can facilitate its wetting in water solutions. PN-ECB samples synthesized at lower temperatures were also investigated (Figure S6). The specific capacitances of samples PN-ECB-850 and PN-ECB-750, obtained from galvanostatic charge/discharge curves at a current density of 2.0 A g^{-1} , are much lower compared to those of PN-ECB-950. The low specific surface area and pore

volume are the main reasons for their reduced specific capacitance. Furthermore, the PN-ECB-950-based supercapacitor exhibited high stability during the charge/discharge cycles. After 10 000 galvanostatic charge/discharge cycles at a current density of 5 A g^{-1} , it can retain 93.5% of its initial specific capacity (Figure 4d).

The electrode with high active mass loading is important for a high packing factor of the capacitor.⁴⁹ Nevertheless, a high mass loading of active materials on the current collector will unavoidably increase the thickness of the electrode and thus influence the migration rate of the ions from the electrolyte inside the electrode materials. To investigate the mass loading effect of active materials on the performance of the capacitor, we fabricated a series of prototype supercapacitors with different electrode mass loading of active materials. For PN-ECB-950, with mass loading increased from 1.57 to 6.42 mg cm^{-2} , the CV curves (obtained at a scanning rate of 100 mV s^{-1}) can retain nearly symmetrical rectangular shapes (Figure 5a) and the electrode can retain 95% of its initial capacitance (obtained at a discharge rate of 2 A g^{-1}) (Figure S7). These results suggest that high rate performance can be maintained with a high mass loading for sample PN-ECB-950. For comparison, the CV curve of commercial AC made the electrode to deviate from rectangular shape at a moderate electrode mass loading (4.15 mg cm^{-2}), and the specific capacitance was much lower compared to that of PN-ECB-950, with similar electrode mass loading. Further, electrochemical impedance spectroscopy experiment was conducted to investigate the kinetics of these electrodes. Figure 5b presents

the Nyquist plot of capacitors fabricated with commercial AC and PN-ECB-950 of different electrode mass loading. Clearly, all of these plots feature vertical curves at low frequencies, indicating their ideal capacitive behavior.⁴⁸ PN-ECB-950-based capacitor samples show a relative lower series resistance (about $0.7 \Omega \text{ cm}^2$) compared to that of the AC-based one ($1 \Omega \text{ cm}^2$), suggesting their improved electronic conductivity. Notably, large differences were observed at medium frequencies, where the plots transfer from a vertical curve to a 45 Warburg region and a semicircle region, corresponding to the electrolyte-diffusion resistance and charge-transfer resistance in the electrode. For PN-ECB-950-based capacitors with various electrode mass loading, the 45 Warburg region is negligible, suggesting their efficient ion transport even in thick electrodes.⁵⁰ Nevertheless, the diameter of the semicircle increases linearly with the electrode mass loading, which suggests that the charge-transfer resistance is the main reason for the decrease in the capacitance of the capacitor with high electrode mass loading. The AC-based capacitor exhibits a much larger 45 Warburg region and a similar semicircle region compared to those of the PN-ECB-950-based capacitor of similar electrode mass loading, suggesting that its capacitance performance is mainly limited by the electrolyte ion-transport rate rather than the charge-transfer resistance in the electrode. Impedance phase angle data of these capacitors are shown in Figure 5c. The relaxation time constant (τ_0), defined as the inverse of frequency (f_0) at a phase angle of 45° (the point where the resistive and capacitive impedances are equal),⁵⁰ reached 0.16 s for the PN-ECB-950-based capacitor with a mass loading of 1.57 mg cm^{-2} . The time constant increases slowly with the electrode mass loading and reaches 1.10 s for an ultrahigh mass loading electrode (12.38 mg cm^{-2}), which is still lower than that of AC-based capacitor with only about one-third of its electrode mass loading (4.15 mg cm^{-2}). These results further indicate the excellent ion-transport rate of PN-ECB-950-based capacitor even for electrode with high mass loading. The Ragone plot of PN-ECB-950-based capacitor (electrode mass loading, 2.14 mg cm^{-2}) is shown in Figure 5d. It presents much higher average power density and energy density than the AC-based one, especially at short current drain times. The result is also among the best of all recently reported aqueous-based high-rate supercapacitors, including supercapacitors based on micro/mesohierarchical porous graphitic carbon (HGPC),¹⁵ three-dimensional reduced graphene oxide hydrogel,^{16,36,51} mesopore-dominant interconnected strutted graphene,¹⁷ and other reported three-dimensional porous carbons.³⁵

The high capacitive behavior of sample PN-ECB-950 can be ascribed to its unique surface chemistry and microstructure. On the one hand, the vertically aligned porous graphene layers provide both large accessible surface area for the adsorption and desorption of electrolyte ion and fast pathways for the mobility of the electrolyte ions during the charge/discharge process, which enables both high specific capacitance and high rate capability. On the other hand, the abundant nitrogen heteroatoms and phosphorus functional groups in the host material can provide additional pseudocapacitance, further improving the capacitance properties.^{22,25} Additionally, the surface phosphorus functional groups can improve the surface wettability of the electrode in aqueous electrolyte solution, which is probably another reason for the improved capacitance of PN-ECB-950.

4. CONCLUSIONS

In conclusion, we successfully synthesized a novel porous carbon that is made up of aligned exfoliated pore-rich carbon nanosheets of thickness of a few nanometers. Experimental results indicate that the optimized sample, PN-ECB-950, enriched with nitrogen dopants in the basal plane and phosphorus functional groups at the edge of graphene lattice, shows high specific capacitance and excellent rate performance as supercapacitor materials. The open porous framework formed by the well-defined neighboring interlayer space of thin graphite walls not only provides large electrode–electrolyte interfaces for electrochemical reaction but also reduces the diffusive resistance by affording fast pathways for ion transport. Particularly, the enhanced electrochemical characteristics were maintained even when the electrode mass loading increased, which we attributed to the vertically aligned pore structure of the synthesized porous carbon sheets.

■ ASSOCIATED CONTENT

Supporting Information

The Supporting Information is available free of charge on the ACS Publications website at DOI: 10.1021/acsami.7b00617.

Raman spectra of sample PN-ECB-950; XRD pattern of sample PN-ECB-950; SEM image of sample N-ECB-950 without adding acid to the precursor; TEM image of sample PC-950 without adding melamine to the precursor; nitrogen adsorption and desorption isotherms, and pore-size distribution of samples PN-ECB-650, PN-ECB-750, PN-ECB-850, PN-ECB-950, and N-ECB-950; galvanostatic charge/discharge curves of samples N-ECB-950, PN-ECB-850, and PN-ECB-750 at a constant current density of 2 A g^{-1} ; dependence of the specific capacitance of PN-ECB-950 on mass loading (Figures S1–S7); chemical composition of the synthesized samples (Table S1) (PDF)

■ AUTHOR INFORMATION

Corresponding Authors

*E-mail: lifeng.cui@gmail.com (L.C.).

*E-mail: fhb@dgut.edu.cn (H.F.).

ORCID

Jutao Jin: 0000-0003-0523-0895

Zhong-Shuai Wu: 0000-0003-1851-4803

Author Contributions

This article was written through contributions of all authors. All authors have given approval to the final version of the manuscript.

Funding

This study was financially supported by the National Basic Research Program of China (2012CB215500), the National Nature Science Foundation (NSFC) of China under award no. 50823008, and DICP Fundamental Research Program for Clean Energy (2013D102)

Notes

The authors declare no competing financial interest.

■ REFERENCES

- (1) Miller, J. R.; Simon, P. Electrochemical Capacitors for Energy Management. *Science* **2008**, *321*, 651–652.
- (2) Qie, L.; Chen, W.; Xu, H.; Xiong, X.-Q.; Jiang, Y.; Zou, F.; Hu, X.; Xin, Y.; Zhang, Z.; Huang, Y. Synthesis of Functionalized 3D

Hierarchical Porous Carbon for High-Performance Supercapacitor. *Energy Environ. Sci.* **2013**, *6*, 2497–2504.

(3) Hulicova-Jurcakova, D.; Puziy, A. M.; Poddubnaya, O. I.; Suárez-García, F.; Tascón, J. M. D.; Lu, G. Q. Highly Stable Performance of Supercapacitors from Phosphorus-Enriched Carbons. *J. Am. Chem. Soc.* **2009**, *131*, 5026–5027.

(4) Borchardt, L.; Oschatz, M.; Kaskel, S. Tailoring Porosity in Carbon Materials for Supercapacitor Applications. *Mater. Horiz.* **2014**, *1*, 157–168.

(5) Liu, C.; Yu, Z.; Neff, D.; Zhamu, A.; Jang, B. Z. Graphene-Based Supercapacitor with an Ultrahigh Energy Density. *Nano Lett.* **2010**, *10*, 4863–4868.

(6) Chmiola, J.; Yushin, G.; Gogotsi, Y.; Portet, C.; Simon, P.; Taberna, P. L. Anomalous Increase in Carbon Capacitance at Pore Sizes Less Than 1 Nanometer. *Science* **2006**, *313*, 1760–1763.

(7) Lin, T.; Chen, I.-W.; Liu, F.; Yang, C.; Bi, H.; Xu, F.; Huang, F. Nitrogen-Doped Mesoporous Carbon of Extraordinary Capacitance for Electrochemical Energy Storage. *Science* **2015**, *350*, 1508–1513.

(8) Zhu, Y.; Murali, S.; Stoller, M. D.; Ganesh, K. J.; Cai, W.; Ferreira, P. J.; Pirkle, A.; Wallace, R. M.; Cychosz, K. A.; Thommes, M.; Su, D.; Stach, E. A.; Ruoff, R. S. Carbon-Based Supercapacitors Produced by Activation of Graphene. *Science* **2011**, *332*, 1537–1541.

(9) Wang, R.; Wang, P.; Yan, X.; Lang, J.; Peng, C.; Xue, Q. Promising Porous Carbon Derived from Celtsuce Leaves with Outstanding Supercapacitance and CO₂ Capture Performance. *ACS Appl. Mater. Interfaces* **2012**, *4*, 5800–5806.

(10) Mondal, A. K.; Kretschmer, K.; Zhao, Y.; Liu, H.; Wang, C.; Sun, B.; Wang, G. Nitrogen-Doped Porous Carbon Nanosheets from Eco-Friendly Eucalyptus Leaves as High Performance Electrode Materials for Supercapacitors and Lithium Ion Batteries. *Chem. – Eur. J.* **2017**, *23*, 3683–3690.

(11) Simon, P.; Gogotsi, Y. Capacitive Energy Storage in Nanostructured Carbon–Electrolyte Systems. *Acc. Chem. Res.* **2013**, *46*, 1094–110.

(12) To, J. W. F.; Chen, Z.; Yao, H.; He, J.; Kim, K.; Chou, H.-H.; Pan, L.; Wilcox, J.; Cui, Y.; Bao, Z. Ultrahigh Surface Area Three-Dimensional Porous Graphitic Carbon from Conjugated Polymeric Molecular Framework. *ACS Cent. Sci.* **2015**, *1*, 68–76.

(13) Choi, B. G.; Yang, M.; Hong, W. H.; Choi, J. W.; Huh, Y. S. 3D Macroporous Graphene Frameworks for Supercapacitors with High Energy and Power Densities. *ACS Nano* **2012**, *6*, 4020–4028.

(14) Xu, Y.; Lin, Z.; Huang, X.; Wang, Y.; Huang, Y.; Duan, X. Functionalized Graphene Hydrogel-Based High-Performance Supercapacitors. *Adv. Mater.* **2013**, *25*, 5779–5784.

(15) Wang, D.-W.; Li, F.; Liu, M.; Lu, G. Q.; Cheng, H.-M. 3D Aperiodic Hierarchical Porous Graphitic Carbon Material for High-Rate Electrochemical Capacitive Energy Storage. *Angew. Chem., Int. Ed.* **2008**, *47*, 373–376.

(16) Wu, Z.-S.; Sun, Y.; Tan, Y.-Z.; Yang, S.; Feng, X.; Mullen, K. Three-Dimensional Graphene-based Macro- and Meso-porous Frameworks for High Performance Electrochemical Capacitive Energy Storage. *J. Am. Chem. Soc.* **2012**, *134*, 19532–19535.

(17) Wang, X.; Zhang, Y.; Zhi, C.; Wang, X.; Tang, D.; Xu, Y.; Weng, Q.; Jiang, X.; Mitome, M.; Golberg, D.; Bando, Y. Three-Dimensional Struttated Graphene Grown by Substrate-Free Sugar Blowing for High-Power-Density Supercapacitors. *Nat. Commun.* **2013**, *4*, No. 2905.

(18) Xu, Y.; Lin, Z.; Zhong, X.; Huang, X.; Weiss, N. O.; Huang, Y.; Duan, X. Holey Graphene Frameworks for Highly Efficient Capacitive Energy Storage. *Nat. Commun.* **2014**, *5*, No. 4554.

(19) Hulicova-Jurcakova, D.; Kodama, M.; Shiraishi, S.; Hatori, H.; Zhu, Z. H.; Lu, G. Q. Nitrogen-Enriched Nonporous Carbon Electrodes with Extraordinary Supercapacitance. *Adv. Funct. Mater.* **2009**, *19*, 1800–1809.

(20) Wang, D.-W.; Li, F.; Yin, L.-C.; Lu, X.; Chen, Z.-G.; Gentle, I. R.; Lu, G. Q.; Cheng, H.-M. Nitrogen-Doped Carbon Monolith for Alkaline Supercapacitors and Understanding Nitrogen-Induced Redox Transitions. *Chem. – Eur. J.* **2012**, *18*, 5345–5351.

(21) Carriazo, D.; Gutiérrez, M. C.; Picó, F.; Rojo, J. M.; Fierro, J. L. G.; Ferrer, M. L.; del Monte, F. Phosphate-Functionalized Carbon

Monoliths from Deep Eutectic Solvents and their Use as Monolithic Electrodes in Supercapacitors. *ChemSusChem* **2012**, *5*, 1405–1409.

(22) Zhang, L.; Zhao, X.; Ji, H.; Stoller, M.; Lai, L.; Murali, S.; McDonnell, S.; Cleveger, B.; Wallace, R. M.; Ruoff, R. Nitrogen Doping of Graphene and its Effect on Quantum Capacitance, and a New Insight on the Enhanced Capacitance of N-doped Carbon. *Energy Environ. Sci.* **2012**, *5*, 9618–9625.

(23) Zheng, C.; Zhou, X. F.; Cao, H. L.; Wang, G. H.; Liu, Z. P. Edge-Enriched Porous Graphene Nanoribbons for High Energy Density Supercapacitors. *J. Mater. Chem. A* **2014**, *2*, 7484–7490.

(24) Yan, X.; Liu, Y.; Fan, X.; Jia, X.; Yu, Y.; Yang, X. Nitrogen/Phosphorus Co-doped Nonporous Carbon Nanofibers for High-Performance Supercapacitors. *J. Power Sources* **2014**, *248*, 745–751.

(25) Jeong, H. M.; Lee, J. W.; Shin, W. H.; Choi, Y. J.; Shin, H. J.; Kang, J. K.; Choi, J. W. Nitrogen-Doped Graphene for High-Performance Ultracapacitors and the Importance of Nitrogen-Doped Sites at Basal Planes. *Nano Lett.* **2011**, *11*, 2472–2477.

(26) Stoller, M. D.; Park, S. J.; Zhu, Y. W.; An, J. H.; Ruoff, R. S. Graphene-Based Ultracapacitors. *Nano Lett.* **2008**, *8*, 3498–3502.

(27) Xu, B.; Wu, F.; Chen, S.; Zhang, C.; Cao, G.; Yang, Y. Activated Carbon Fiber Cloths as Electrodes for High Performance Electric Double Layer Capacitors. *Electrochim. Acta* **2007**, *52*, 4595–4598.

(28) Xu, B.; Wu, F.; Chen, R.; Cao, G.; Chen, S.; Yang, Y. Mesoporous Activated Carbon Fiber as Electrode Material for High-Performance Electrochemical Double Layer Capacitors with Ionic Liquid Electrolyte. *J. Power Sources* **2010**, *195*, 2118–2124.

(29) Hou, J.; Cao, C.; Idrees, F.; Ma, X. Hierarchical Porous Nitrogen-Doped Carbon Nanosheets Derived from Silk for Ultrahigh-Capacity Battery Anodes and Supercapacitors. *ACS Nano* **2015**, *9*, 2556–2564.

(30) Liang, Q.; Yao, X.; Wang, W.; Liu, Y.; Wong, C. P. A Three-Dimensional Vertically Aligned Functionalized Multilayer Graphene Architecture: An Approach for Graphene-Based Thermal Interfacial Materials. *ACS Nano* **2011**, *5*, 2392–2401.

(31) Sevilla, M.; Fuertes, A. B. Direct Synthesis of Highly Porous Interconnected Carbon Nanosheets and Their Application as High-Performance Supercapacitors. *ACS Nano* **2014**, *8*, 5069–5078.

(32) Wang, H.; Xu, Z.; Kohandehghan, A.; Li, Z.; Cui, K.; Tan, X.; Stephenson, T. J.; King'ondo, C. K.; Holt, C. M. B.; Olsen, B. C.; Tak, J. K.; Harfield, D.; Anyia, A. O.; Mitlin, D. Interconnected Carbon Nanosheets Derived from Hemp for Ultrafast Supercapacitors with High Energy. *ACS Nano* **2013**, *7*, 5131–5141.

(33) Yoon, Y.; Lee, K.; Kwon, S.; Seo, S.; Yoo, H.; Kim, S.; Shin, Y.; Park, Y.; Kim, D.; Choi, J.-Y.; Lee, H. Vertical Alignments of Graphene Sheets Spatially and Densely Piled for Fast Ion Diffusion in Compact Supercapacitors. *ACS Nano* **2014**, *8*, 4580–4590.

(34) Li, Z.; Zhang, L.; Amirkhiz, B. S.; Tan, X.; Xu, Z.; Wang, H.; Olsen, B. C.; Holt, C. M. B.; Mitlin, D. Carbonized Chicken Eggshell Membranes with 3D Architectures as High-Performance Electrode Materials for Supercapacitors. *Adv. Energy Mater.* **2012**, *2*, 431–437.

(35) Chen, L.-F.; Huang, Z.-H.; Liang, H.-W.; Gao, H.-L.; Yu, S.-H. Three-Dimensional Heteroatom-Doped Carbon Nanofiber Networks Derived from Bacterial Cellulose for Supercapacitors. *Adv. Funct. Mater.* **2014**, *24*, 5104–5111.

(36) Wu, Z.-S.; Winter, A.; Chen, L.; Sun, Y.; Turchanin, A.; Feng, X.; Müllen, K. Three-Dimensional Nitrogen and Boron Co-doped Graphene for High-Performance All-Solid-State Supercapacitors. *Adv. Mater.* **2012**, *24*, 5130–5135.

(37) Jiang, H.; Lee, P. S.; Li, C. Three-dimensional carbon based nanostructures for advanced supercapacitors. *Energy Environ. Sci.* **2013**, *6*, 41–53.

(38) Wang, P.; He, H.; Xu, X.; Jin, Y. Significantly Enhancing Supercapacitive Performance of Nitrogen-doped Graphene Nanosheet Electrodes by Phosphoric Acid Activation. *ACS Appl. Mater. Interfaces* **2014**, *6*, 1563–1568.

(39) Jin, J.; Gu, L.; Jiang, L.; Liu, J.; Sun, G. A Direct Phase Separation Approach Synthesis of Hierarchically Porous Functional Carbon as an Advanced Electrocatalyst for Oxygen Reduction Reaction. *Carbon* **2016**, *109*, 306–313.

- (40) Wang, C.; Zhou, Y.; Sun, L.; Zhao, Q.; Zhang, X.; Wan, P.; Qiu, J. N/P-Codoped Thermally Reduced Graphene for High-Performance Supercapacitor Applications. *J. Phys. Chem. C* **2013**, *117*, 14912–14919.
- (41) Wang, H.; Maiyalagan, T.; Wang, X. Review on Recent Progress in Nitrogen-Doped Graphene: Synthesis, Characterization, and Its Potential Applications. *ACS Catal.* **2012**, *2*, 781–794.
- (42) Pels, J. R.; Kapteijn, F.; Moulijn, J. A.; Zhu, Q.; Thomas, K. M. Evolution of Nitrogen Functionalities in Carbonaceous Materials during Pyrolysis. *Carbon* **1995**, *33*, 1641–1653.
- (43) Puziy, A. M.; Poddubnaya, O. I.; Martínez-Alonso, A.; Suárez-García, F.; Tascón, J. M. D. Synthetic Carbons Activated with Phosphoric acid: I. Surface Chemistry and Ion Binding Properties. *Carbon* **2002**, *40*, 1493–1505.
- (44) Puziy, A. M.; Poddubnaya, O. I.; Martínez-Alonso, A.; Suárez-García, F.; Tascón, J. M. D. Synthetic Carbons Activated with Phosphoric Acid: II. Porous Structure. *Carbon* **2002**, *40*, 1507–1519.
- (45) Puziy, A. M.; Poddubnaya, O. I.; Socha, R. P.; Gurgul, J.; Wisniewski, M. XPS and NMR Studies of Phosphoric Acid Activated Carbons. *Carbon* **2008**, *46*, 2113–2123.
- (46) Zhang, J.; Liu, X.; Blume, R.; Zhang, A.; Schlögl, R.; Su, D. S. Surface-Modified Carbon Nanotubes Catalyze Oxidative Dehydrogenation of n-Butane. *Science* **2008**, *322*, 73–77.
- (47) Puziy, A. M.; Poddubnaya, O. I.; Martínez-Alonso, A.; Suárez-García, F.; Tascón, J. M. D. Surface Chemistry of Phosphorus-Containing Carbons of Lignocellulosic Origin. *Carbon* **2005**, *43*, 2857–2868.
- (48) Some, S.; Kim, J.; Lee, K.; Kulkarni, A.; Yoon, Y.; Lee, S.; Kim, T.; Lee, H. Highly Air-Stable Phosphorus-Doped n-Type Graphene Field-Effect Transistors. *Adv. Mater.* **2012**, *24*, 5481–5486.
- (49) Awala, H.; Gilson, J.-P.; Retoux, R.; Boullay, P.; Goupil, J.-M.; Valtchev, V.; Mintova, S. Template-free nanosized faujasite-type zeolites. *Nat. Mater.* **2015**, *14*, 447–451.
- (50) Taberna, P. L.; Simon, P.; Fauvarque, J. F. Electrochemical Characteristics and Impedance Spectroscopy Studies of Carbon-Carbon Supercapacitors. *J. Electrochem. Soc.* **2003**, *150*, A292–A300.
- (51) Xu, Y.; Lin, Z.; Huang, X.; Liu, Y.; Huang, Y.; Duan, X. Flexible Solid-State Supercapacitors Based on Three-Dimensional Graphene Hydrogel Films. *ACS Nano* **2013**, *7*, 4042–4049.